

A Facile Approach to Fabricate an N-Doped Mesoporous Graphene/Nanodiamond Hybrid Nanocomposite with Synergistically Enhanced Catalysis

Zhongkui Zhao,* Yitao Dai, Guifang Ge, Qing Mao, Zeming Rong, and Guiru Wang^[a]

Owing to their unique structural features and surface properties, graphene and nanodiamond have attracted tremendous attention in diverse fields. However, restacking of graphene and reagglomeration of dispersed nanodiamond inevitably depress their catalytic properties. Herein, inspired by the historic discovery of “pillared clay”, we successfully realized the simultaneous inhibition of their restacking by fabricating a N-doped mesoporous graphene/nanodiamond (N-RGO/ND) nanocomposite by a facile wet-chemical approach. The electrocatalytic oxygen reduction reaction (ORR) and the thermocatalytic oxidant-free and steam-free direct dehydrogenation (DDH) of ethylbenzene were used to examine its catalytic properties. The nanocomposite showed synergistically improved catalytic DDH and electrocatalytic ORR activity relative to that of the individual components, which can be ascribed to synergy between graphene and nanodiamond and to the large surface area, well-ordered mesoporous structure, small crystalline size, and rich defect and C=O surface features. Moreover, the developed synthetic strategy in this work can be extended to diverse N-doped nanocomposites from dispersion-required carbon precursors.

The development of low-costing sustainable catalysts with high catalytic activity, selectivity, and stability under mild conditions remains at the heart of modern materials chemistry, green chemistry, and catalysis.^[1] Although metal-based catalysts currently play major roles in various industrial production processes, they still suffer from many competitive disadvantages, including low availability, high cost, susceptibility to gas poisoning, and detrimental effects on our environment. Owing to their broad availability, environmental acceptability, corrosion resistance, and unique surface properties, nanocarbon materials have been demonstrated to be promising and sustainable low-costing metal-free alternatives to metal-based catalysts for organic synthesis,^[2] hydrogen production by water splitting,^[3] the photodegradation of organic pollutants,^[4] and the crucial oxygen reduction reaction in fuel cells.^[5] Nowadays, carbocatalysis, especially graphene-based catalysis, has attract-

ed worldwide attention, and it has become the foreland and a hot topic in heterogeneous catalysis, sustainable chemistry, and energy conversion.^[6]

Graphene, a single-atom-thick layer, 2D, pseudoinfinite nanocrystal comprising sp²-hybridized carbon atoms with a covalently packed honeycomb-like lattice structure, has attracted tremendous attention since the direct observation and characterization of a mechanically exfoliated graphene monolayer in 2004, owing to its unique properties, which include a super-large theoretical specific surface area (2630 m²g⁻¹), high thermal conductivity, tunable optical and electronic properties, and excellent mechanical stiffness.^[7] Highly efficient thermo- and electrocatalysis have been investigated.^[2-6] However, the strong π - π stacking interactions that exist between graphene nanosheets can lead to serious aggregation and restacking, which inevitably depresses its catalytic properties, as it inevitably decreases the number of catalytically active sites exposed to the substrates; furthermore, the mass-transfer problem of graphene-based catalysts resulting from nanosheet restacking can also significantly hamper the catalytic activity of these catalysts.^[8] Therefore, seeking a facile and efficient method to minimize the restacking effect and to improve the application properties of graphene-based catalysts is highly desirable but still remains a challenge. Inspired by the historic discovery process of the so-called “pillared clays” that were used in industrial catalysis roughly 80 years ago by inserting some spherical nanoobjects (e.g., Keggin ions) to avoid restacking of bedded clays, we envisioned that the restacking issue of exfoliated graphene nanosheets could be inhibited by inserting spherical carbon materials.

Then, which kinds of spherical carbon should be chosen? Nanodiamond (ND) powder consists of individual diamond nanospheres with an average diameter of 5 nm; it was first produced in the 1960s in the USSR from soot formed in explosions.^[9] Over the past decade, owing to their unique sp³/sp² core-shell structure, highly oxidized surface, large surface-to-volume ratio, high thermal and mechanical stability, exceptional hardness, superior thermal conductivity, wide band gap, good optoelectronic properties, and biocompatibility, ND materials have attracted a great deal of attention for their promising applications in diverse fields, including chemical catalysis and photocatalysis.^[2a,10] NDs have been used as an isolation component between graphene oxide sheets.^[8e] Therefore, ND was selected in this work to inhibit the restacking of exfoliated graphene. Unfortunately, the surface force and chemical bonding force of nanodiamond result in its agglomeration,^[11] which significantly decreases its potential uses. The use of ultrasoni-

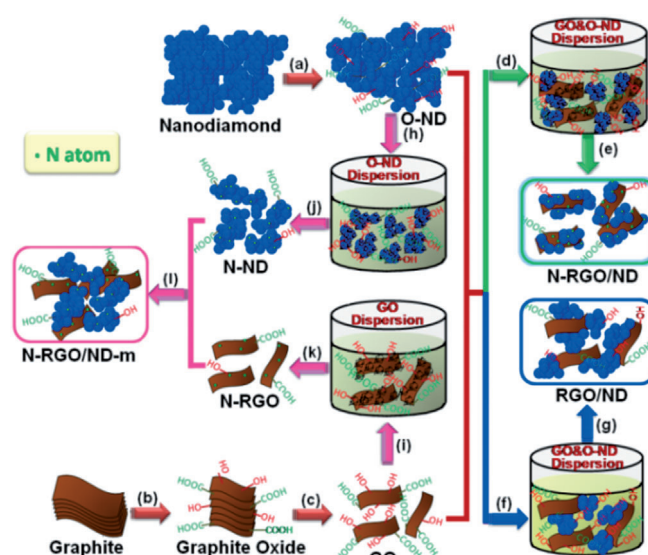
[a] Prof. Z. Zhao, Dr. Y. Dai, Dr. G. Ge, Dr. Q. Mao, Dr. Z. Rong, Prof. G. Wang
State Key Laboratory of Fine Chemicals
School of Chemical Engineering
Dalian University of Technology
2 Linggong Road, Dalian 116024 (P.R. China)
E-mail: zkzhao@dlut.edu.cn

Supporting Information for this article is available on the WWW under
<http://dx.doi.org/10.1002/cctc.201500074>.

ation alone generally does not efficiently work on dispersing ND aggregates that are less than 1 μm in size, and therefore, the development of an efficient method to disperse ND aggregates into smaller aggregates or even a highly dispersed ND is highly desirable. Thus, we thought to fabricate a reduced graphene oxide/nanodiamond (RGO/ND) hybrid nanocomposite with enhanced catalysis on the basis of a synergistic effect, and simultaneously, we would inhibit restacking of exfoliated graphene nanosheets and the reagglomeration of deagglomerated nanodiamond through the interseparating effect of dispersed graphene nanosheets and nanodiamond. As a result, improved catalytic performance should be obtained. More importantly, nitrogen-doping of graphene, as a simple but efficient approach that can be used to tune catalytic properties at the atomic level through tailoring of electronic properties, has drawn intense interest.^[2d,12] Therefore, a powerful strategy including the possibility of fabricating a N-doped graphene/nanodiamond composite is highly desirable and crucial.

Herein, we report a facile and scalable wet-chemical approach to fabricate a N-doped mesoporous N-doped reduced graphene oxide/nanodiamond (N-RGO/ND) hybrid nanocomposite with high surface area, stable hierarchical structure, and excellent electro- and thermocatalysis behavior by using hexamethylenetetramine (HTM) as both the dispersant and the nitrogen precursor. Through this approach, dispersed and deagglomerated nanodiamond can be inserted into graphene nanosheets, and therefore, the reagglomeration of exfoliated graphene nanosheets and deagglomerated nanodiamond can be simultaneously compressed; furthermore, N atoms can be introduced into the carbon matrix at the same time. By fabricating N-RGO/ND, there are more chemically active sites to be exposed on the surface, and the standard mass-transfer problem of lamellar materials can be overcome; furthermore, synergistically enhanced catalysis can be produced by the formation of a new interface of graphene–nanodiamond. To illustrate the benefits of such a hierarchically structured hybrid carbon nanocomposite in catalysis, the electrocatalytic oxygen reduction reaction (ORR) and thermocatalytic direct dehydrogenation (DDH) of ethylbenzene to styrene under oxidant-free and steam-free conditions were performed. It was found that fabricated mesoporous N-RGO/ND demonstrated synergistically enhanced catalysis in the ORR and DDH reactions, which can be ascribed to the unique structure and surface chemical properties of the nanocomposite.

Scheme 1 illustrates the preparation process. The oxidized nanodiamond (O-ND) was prepared by washing the commercially supplied nanodiamond from Beijing Grish Hitech Co. (China) synthesized by detonation with concentrated sulfonic acid, and this was followed by washing and drying processes. The graphene oxide (GO) was prepared according to the classical Hummers method.^[13] The desired N-RGO/ND hybrid nanoarchitecture was typically prepared simply by ultrasonic mixing of GO and O-ND in the presence of HTM and subsequent thermal reduction with N_2 flowing at 750 $^\circ\text{C}$ for 1 h; the addition of HTM is crucial in this process, as it acts as both a dispersant and a nitrogen precursor. For comparison, the graphene/nanodiamond composite without HTM addition (i.e., RGO/ND) and



Scheme 1. Schematic illustration of the procedure used for the preparation of the N-RGO/ND hybrid nanoarchitecture by using hexamethylenetetramine as the dispersant and the nitrogen precursor. a) Oxidation by concentrated H_2SO_4 . b) Oxidation by concentrated H_2SO_4 , KMnO_4 , and H_2O_2 . c) Ultrasonication. d) Dispersion of GO and O-ND into the HTM/EtOH solution. e) Ultrasonication, rotary evaporation, drying, and then thermal reduction. f) Dispersion of GO and O-ND into EtOH. g) Ultrasonication, rotary evaporation, drying, and then thermal reduction. h) Ultrasonication. i) Ultrasonication. j) Ultrasonication, rotary evaporation, drying, and then thermal reduction. k) Ultrasonication, rotary evaporation, drying, and then thermal reduction. l) Mechanical mixing.

the mixture (N-RGO/ND-m) prepared by mechanically mixing N-doped RGO (N-RGO) and N-doped nanodiamond (N-ND) were also fabricated. By using the same procedure as above except for the absence of HTM, RGO/ND was yielded. N-RGO and N-ND were produced by a procedure similar to that described above by immersing GO and O-ND into a solution of HTM and then exposing them to the above thermal reduction process. N-RGO/ND-m was prepared by mechanically mixing the above-prepared N-RGO and N-ND. The detailed preparation procedure can be found in the Supporting Information.

Field-emission (FE) SEM and TEM measurements were performed to characterize the morphology and structure of the fabricated N-RGO/ND as well as the parent nanodiamond and RGO (Figure 1). As is shown in Figure 1a, the ND exists in the form of an agglomerate, which is consistent with the literature.^[11] Stacked RGO nanosheets were successfully prepared by using a modified Hummers method (Figure 1b,c).^[13] Representative FESEM (Figure 1d) and TEM (Figure 1e) images reveal that the deagglomerated nanodiamond is inserted into the graphene nanosheet to form N-RGO/ND by combining well-dispersed graphene with nanodiamond by using HTM as an efficient dispersant, and therefore, their restacking can be simultaneously inhibited, in comparison with ND presented in Figure 1f. Furthermore, the FESEM images of N-RGO/ND-m (Figure S1a,b; Supporting Information) suggest the sample is not a composite but just a simple and disordered deposition, and furthermore, a bigger nanodiamond agglomerate exists, even though the nanodiamond was well dispersed before thermal

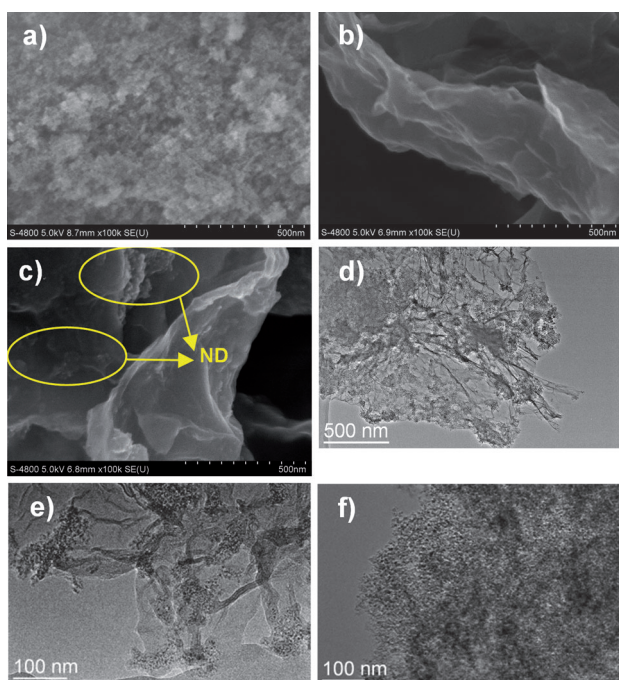


Figure 1. FESEM images of a) ND, b) RGO, and c) the N-RGO/ND hybrid nanoarchitectures (scale bars = 500 nm). TEM images of d, e) N-RGO/ND and f) ND.

reduction; this illustrates that reagglomeration of dispersed nanodiamond takes place in the heating process. The results further confirm that the deagglomerated nanodiamond can be efficiently inhibited by the formation of the graphene/nanodiamond nanocomposite. Comparing the images of RGO/ND (Figure S1 c, d) with those of N-RGO/ND, insertion of the extremely large nanodiamond agglomerate into the graphene nanosheet can be observed, which suggests that the dispersant role of HTM is essential in the formation of the N-RGO/ND nanoarchitecture containing well-dispersed nanodiamond.

The surface area and porosity of N-RGO/ND may offer clear evidence for the formation of the carbon nanocomposite. Therefore, we performed nitrogen adsorption experiments, and the nitrogen-adsorption isotherms and the pore-size distribution from the adsorption branch of N-RGO/ND, ND, and RGO are presented in Figure 2 a, b. The higher surface area of N-RGO/ND ($470.9 \text{ m}^2 \text{ g}^{-1}$) relative to that of RGO (obtained by thermal reduction of GO powder, $306.8 \text{ m}^2 \text{ g}^{-1}$) and to that of ND ($318.6 \text{ m}^2 \text{ g}^{-1}$) from the N_2 adsorption/desorption measurements provides definite evidence for the formation of the composite nanostructure, which prevents restacking and reagglomeration of graphene and nanodiamond. All of the isotherms are type IV according to IUPAC classification, and they exhibit H1 hysteresis with a featured capillary condensation in the mesopores (Figure 3 a), which suggests the presence of

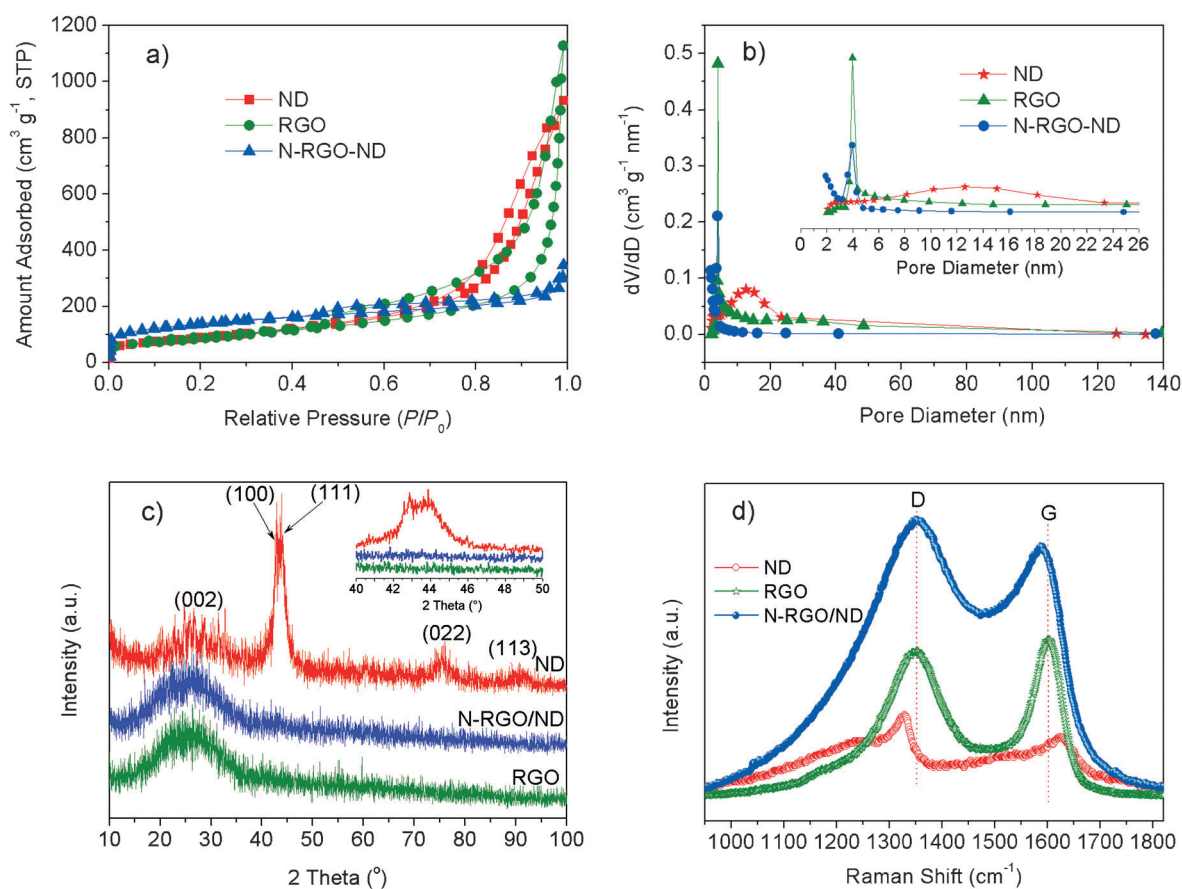


Figure 2. a) Nitrogen adsorption/desorption isotherms. b) BJH pore-size distribution from desorption branch; inset: magnified pore-size distribution. c) XRD patterns; inset: magnified region. d) Raman spectra of the N-RGO/ND, RGO, and ND.

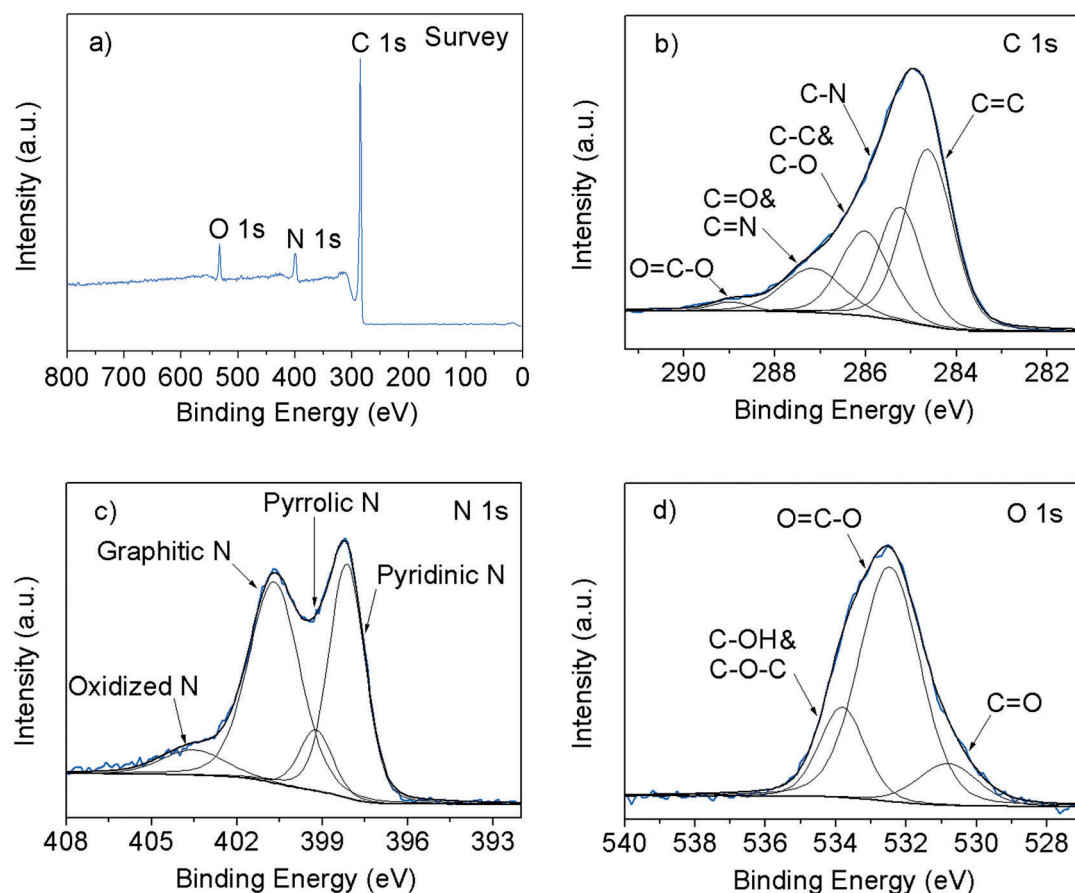


Figure 3. XPS spectra of the as-prepared N-RGO/ND sample: a) Survey, b) C 1s, c) N 1s, and d) O 1s.

well-ordered mesopores in the three samples. Moreover, the smaller pore volume of the composite relative to that of the single components is indicative of the insertion of nanodiamond into the graphene nanosheets to fill the larger accumulating pores, and this indicates the formation of a 3D nanostructure. Interestingly, from Figure 3b, N-RGO/ND shows a narrow pore-size distribution and the pore diameter is small, but graphene and nanodiamond have a broad pore-size distribution along with the presence of larger mesopores and even macropores resulting from the insertion of ND into the graphene nanosheets. The disappearance of the larger accumulated mesopores and macropores of ND and RGO in the composite can be ascribed to deaggregation of ND and the filling of dispersed ND into the RGO nanosheets, respectively. The pore architecture of the three samples and the higher surface area of the N-RGO/ND composite further confirm the formation of a carbon nanocomposite, which efficiently hampers restacking of the graphene nanosheets and dispersed ND. These mesopores are expected to facilitate diffusion of the reactants in the ORR and DDH processes.

X-ray diffraction (XRD) analyses also present the stacking structural information of N-RGO/ND, RGO, and nanodiamond (Figure 2c). Besides the characteristic diffraction peaks located at $2\theta = 42.9$, 43.9 , 75.5 , and 91.0° corresponding to the (100), (111), (022), and (113) diffraction planes of nanodiamond, a broad peak at $2\theta = 26.3^\circ$ corresponding to stacked graphene

sheets on the diamond shell can also be clearly resolved.^[14] For RGO and the developed N-RGO/ND, a broad diffraction peak at $2\theta = 26.3^\circ$, corresponding to well-exfoliated graphene nanosheets, can be observed, but there is a lack of a diffraction peak at approximately $2\theta = 12^\circ$, corresponding to stacked crystallinity of aligned GO this is indicative of the high quality of the synthesized graphene and the graphene-based composite through thermal reduction.^[15] Through circumspective analysis of the peak at $2\theta = 26.3^\circ$ for RGO and N-RGO/ND, the peak for N-RGO/ND is much weaker and broader, which is indicative of the restacking-inhibited characteristic of N-RGO/ND.^[5a,8a,16] The widened and less-intense peak at $2\theta = 43.9^\circ$ corresponding to the (111) plane of nanodiamond on the composite is indicative of the reagglomeration-inhibited feature of the deagglomerated nanodiamond inserted into the graphene nanosheets,^[14] this is in agreement with the results obtained from FESEM. Furthermore, in comparison to the (111) plane characteristic peak at $2\theta = 43.9^\circ$ for nanodiamond in N-RGO/ND-m and RGO/ND (Figure S2), an extremely weak peak is observed for the N-RGO/ND sample, which provides further evidence for the dispersing effect of the wet-chemical approach developed in this work.

Raman spectroscopy was used to further examine the structure of the carbon nanocomposite, besides the nitrogen doping state (Figure 2d; see also Figures S3 and S4). The Raman spectrum of N-RGO/ND exhibits four feature bands in

the $\tilde{\nu}=1000\text{--}3000\text{ cm}^{-1}$ range and consists of a well-defined D band ($\tilde{\nu}=1353\text{ cm}^{-1}$, corresponding to defective and disordered graphene), G band ($\tilde{\nu}=1600\text{ cm}^{-1}$, corresponding to pristine graphene), 2D band ($\tilde{\nu}=2697\text{ cm}^{-1}$, corresponding to the overtone of the D band produced from a two-phonon scattering process), and D + G bands ($\tilde{\nu}=2930\text{ cm}^{-1}$), which is similar to the characteristics of RGO (Figure 1d; see also Figure S3); this suggests the existence of well-exfoliated graphene nanosheets in both samples.^[17] However, close comparison of their features reveals broadened and strengthened D and 2D bands for N-RGO/ND, which provides evidence for more disorder and more defective graphene nanosheets on the composite resulting from inhibition of reagglomeration of the graphene nanosheet by incorporation of nanodiamond, as no disordered graphene exists on the nanodiamond alone as confirmed by the absence of D and 2D feature bands for the nanodiamond.^[17c-e] Moreover, the Raman band corresponding to the G band in the N-RGO/ND composite is visibly downshifted from $\tilde{\nu}=1605$ to 1587 cm^{-1} with respect to that in RGO, whereas the position of the D band in both N-RGO/ND and RGO remains unchanged at $\tilde{\nu}=1353\text{ cm}^{-1}$. This phenomenon can be ascribed to nitrogen doping in the carbon matrix of the composite; this is consistent with the results of nitrogen-doped graphene and nitrogen-doped carbon nanotubes.^[17a-c,e,18] Furthermore, the I_D/I_G ratio, which is the ratio of the intensities of the D and G bands, provides a sensitive measure of the disorder and crystallite size of the graphene layers (Figure S4). The I_D/I_G ratio of N-RGO/ND (1.12) is much higher than that of RGO (0.92), which suggests that there is more disorder in the composite and that the crystallite size of the nanosheets is smaller.^[16a,17b,c] We calculated the in-plane crystallite sizes (L_a) of N-RGO/ND, RGO, N-RGO/ND-m, and RGO/ND by using Equation (1):^[17]

$$L_a [\text{nm}] = (2.4 \times 10^{-10}) \lambda^4 \left(\frac{I_D}{I_G}\right)^{-1} \quad (1)$$

in which λ is the Raman excitation wavelength (532 nm).

The crystallite sizes of the N-RGO/ND, RGO, N-RGO/ND-m, and RGO/ND samples are estimated to be 17.2, 20.9, 20.2, and 18.1 nm, respectively. The smaller crystallite sizes of RGO/ND, N-RGO/ND-m, and RGO/ND relative to that of RGO illustrates the inhibiting effect resulting from the wrapped nanodiamond on the graphene nanosheets, which is in agreement with the results obtained from FESEM, N_2 adsorption/desorption, and XRD analysis.

By incorporating the structural characteristics obtained from FESEM, TEM, XRD, and Raman spectroscopy, the interinhibiting effect on restacking of exfoliated graphene and the reagglomeration of deagglomerated nanodiamond has been confirmed. Furthermore, by employing FTIR spectroscopy and X-ray photoelectron spectroscopy (XPS), the surface chemical state of the developed N-RGO/ND composite was measured. The FTIR spectra of N-RGO/ND, RGO, and ND (Figure S5) indicate the existence of surface groups including C=O, C–O, C–H, and CN, which is essential for catalysis application.^[2a-c,15a,17e,19] The survey scan of the XPS analysis (Figure 3a) unambiguously

confirms the presence of nitrogen (8.2 atom%) in the N-RGO/ND sample. The C 1s peak region in the XPS spectrum (Figure 3b) was deconvoluted into five peaks at binding energies of approximately 284.6, 285.2, 286.0, 287.1, and 289.0 eV corresponding to C=C (41.2%, mainly from RGO in the composite), C–N (24.1%), C–C/C–O (20.0%, mainly from ND), C=O/C=N (13.0%), and O–C=O (1.7%), respectively (Table S1, Figure S6),^[2b,c,15a,17b,c,19b,20] which is in good agreement with the FTIR spectroscopy results. The N 1s XPS peak (Figure 3c, see also Figure S7 and Table S2) illustrates that the N atoms from HTM are incorporated into the graphene lattice mainly in a form of “pyridinic N” (37.9%) and “graphitic N” (also called quaternary N, 46.0%), besides 9.0% of pyrrolic N and 7.1% of oxidized N, which appear at binding energies of approximately 398.1, 400.7, 399.2, and 403.5 eV, respectively.^[2b,c,15a,17c,20a,21] The O 1s XPS spectrum can be deconvoluted into three peaks with binding energies of 530.8, 532.5, and 533.8 eV, assigned to C=O (ketonic carbonyl group, 12.0%), O–C–O (sum of carboxylic acid, anhydride, lactone, and ester groups, 68.4%), and C–O–C/C–OH (19.6%) containing groups (Figure 3d, see also Figure S8 and Table S3),^[2a-c,19a,22] which is crucial for its fascinating catalytic performance.

We evaluated the catalytic performance of the samples for the DDH reaction. From Figure 4, the rate of formation of sty-

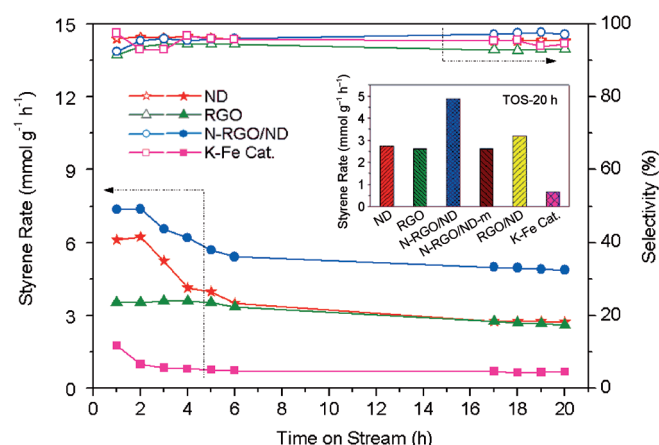


Figure 4. Catalytic performance in the DDH reaction; inset: stable styrene rate, time on stream: 20 h. Reaction conditions: Catalyst (25 mg), 550 °C, 2.8% ethylbenzene in Ar, 10 mL min⁻¹.

rene rapidly drops from 3.5 to 2.6 $\text{mmol g}^{-1}\text{ h}^{-1}$ over pristine RGO and from 6.1 to 2.7 $\text{mmol g}^{-1}\text{ h}^{-1}$ over ND. However, the developed mesoporous N-RGO/ND nanocomposite shows a steady-state styrene rate that is 1.9 and 1.8 times that of the parent RGO and ND, respectively, and that is 7.0 times higher than that of the industrially used K-Fe catalyst; this is ascribed to the high surface area, increased number of catalytically active sites exposed to the substrates, and the intensified mass-transfer of graphene-based catalysts through simultaneously efficient inhibition of restacking the exfoliated graphene nanosheets and re-agglomeration of the dispersed nanodiamond confirmed by the above characterization results. More-

over, the developed nanocomposite also shows higher activity than the mixture containing N-RGO and N-ND, ascribed to synergy between graphene and nanodiamond in the unique mesoporous nanoarchitecture. The promoting effect of nitrogen doping during the nanocomposite preparation process can be observed, and this is in good agreement with our previously reported results.^[2b,c] Relative to the activity of N-RGO/ND, the inferior activity of RGO/ND prepared by the same process except for the absence of HTM implies the dispersion role of HTM and N doping. As reported,^[2a-c,23] surface C=O groups on carbon materials are the catalytically active sites for this reaction. However, from the XPS results (Table S3), the number of C=O groups on the surface of either RGO or ND is larger than that on the N-RGO/ND catalyst (Table S3). It can be proposed that nitrogen incorporated into the carbon matrix, besides the essential synergism confirmed above, may be one reason for this superior activity.^[2b,c,12,19a,20a] Furthermore, we find an interesting phenomenon that RGO/ND prepared by the wet-chemical approach is superior to the mechanically mixed N-RGO/ND-m sample, although the introduction of N is generally favorable for the reaction, which suggests that the formation of an interface between ND and RGO is important. The conclusion can be further evidenced by the fact that the activity of RGO/ND-m is similar to that of pristine ND and RGO.

ORR is an important process in many fields including energy conversion and storage, for example, in fuel cells and metal–air batteries, in addition to other applications such as corrosion, biosensing, and oxygen detection.^[5a,b,12a,17a,24] Herein, the ORR electrocatalytic performance of the as-synthesized samples was first investigated by cyclic voltammetry. From Figures 5a and S9, a quasirectangular voltammogram without any visible peak can be observed for N-RGO/ND in the N₂-saturated solution, whereas distinct ORR responses are observed for all samples in O₂-saturated solution, which is indicative of their ability in the electrocatalytic ORR. Notably, N-RGO/ND shows the highest peak current of 0.52 mA cm⁻², which is markedly higher than that of the other samples including the parent RGO and ND, and even much higher than that of the mixture containing N-RGO and N-ND (N-RGO/ND-m), which suggests that it has much higher catalytic activity. To obtain further insight into the ORR of N-RGO/ND, linear sweep voltammograms on a rotating disc electrode were recorded for N-RGO/ND, N-RGO/ND-m, as well as for the parent RGO and ND. From Figure 5b, a typical two-step pathway is observed for the N-RGO/ND electrode at approximately 0.28 and 0.66 V, which is suggestive of a successive two-electron reaction pathway consistent with the reported boron nanotubes but not the direct four-electron pathway seen for commercially available Pt/C.^[17a] Furthermore, N-RGO/ND shows a more positive onset potential than the others, and this suggests it has higher ORR activity, possibly ascribed to N doping and synergistically enhanced catalysis.^[5a]

In summary, we developed a facile and scalable wet-chemical approach for fabricating a mesoporous N-doped graphene/nanodiamond nanocomposite by using hexamethylenetetramine as both the dispersant and the nitrogen precursor, through which the restacking of well-exfoliated graphene nanosheets and the reaggregation of deagglomerated nano-

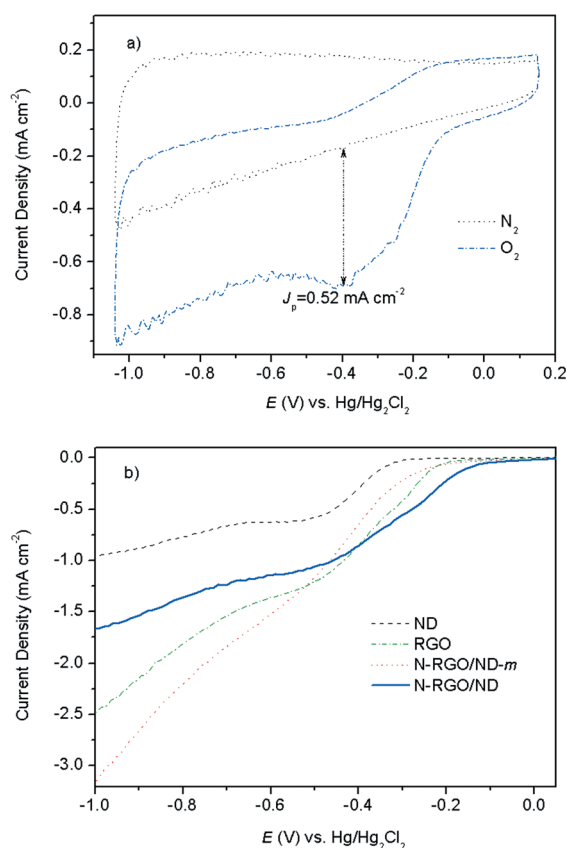


Figure 5. a) Cyclic voltammetry curves of N-RGO/ND in O₂- or N₂-saturated 0.1 M KOH electrolyte at a scan rate of 50 mV s⁻¹. b) Linear sweep voltammograms of diverse samples on a rotating disc electrode at a rotation rate of 1600 rpm and a scan rate of 10 mV s⁻¹.

diamond were simultaneously inhibited. The developed N-doped mesoporous graphene/nanodiamond (N-RGO/ND) carbon nanocomposite showed superior electrocatalysis in the oxygen reduction reaction and better thermocatalytic performance in the direct dehydrogenation reaction than the parent compounds, and this was ascribed to the unique structure and surface chemical properties of the nanocomposite. We believe the N-RGO/ND hybrid nanocomposite could be extended to use in diverse fields with improved applications properties, as both nanodiamond and reduced graphene oxide alone have shown great potential in diverse applications. Furthermore, the synthetic strategy presented in his paper including the wet-chemical approach with hexamethylenetetramine as both the dispersant and the nitrogen precursor can be extended to the fabrication of other nitrogen-doped carbon hybrid nanocomposites from the dispersion-required carbon precursors.

Experimental Section

Synthesis of the catalysts

Graphene oxide (GO) was prepared by the modified Hummers method, and reduced graphene oxide (RGO) was prepared by thermal reduction of GO. Oxidized nanodiamond (O-ND) was prepared

by acid washing the commercially supplied nanodiamond from Beijing Grish Hitech Co. (China) synthesized by the detonation method with acid washing with concentrated sulfonic acid, followed by water washing and drying processes. The N-RGO/ND was synthesized as follows: A desirable amount of HTM was dissolved in ethanol (120 mL) to form a HTM solution. O-ND (30 mg) was added to the HTM solution, and the mixture was dispersed by ultrasonication for 10 min. Subsequently, the obtained GO powder (30 mg) was added into the above O-ND-containing solution. The mixture was treated by further ultrasonication, followed by stirring for 3 h. The solvent was removed under reduced pressure, and the resulting slurry was dried overnight. It was subsequently placed in a quartz tube filled with flowing N_2 gas at $750^\circ C$ for 1 h and was then cooled naturally to room temperature under the protection of N_2 . The finally obtained solid was denoted as N-RGO/ND. By using the same procedure except for the absence of HTM, RGO/ND was yielded. N-RGO and N-ND were produced by a similar procedure by immersing GO and O-ND, respectively. N-RGO/ND-m was prepared by mechanically mixing the above-prepared N-RGO and N-ND.

Characterization of catalysts

X-ray diffraction (XRD) profiles were collected from $2\theta = 10$ to 80° at a step width of 0.02° by using a Rigaku Automatic X-ray Diffractometer (D/Max 2400) equipped with a CuK_{α} source ($\lambda = 1.5406 \text{ \AA}$). Field-emission scanning electron microscopy (FESEM) experiments were performed with a JEOL JSM-5600 LV SEM/EDX instrument. Transmission electron microscopy (TEM) images were obtained by using a Tecnai F30 HRTEM instrument (FEI Corp.) at an acceleration voltage of 300 kV. The XPS spectra were obtained with an ESCALAB 250 XPS system with a monochromated AlK_{α} X-ray source (15 kV, 150 W, $500 \mu m$, pass energy = 50 eV). The Raman spectra were measured by using a laser with an excitation wavelength of 532 nm at room temperature with a Thermo Scientific DXR Raman microscope. FTIR spectroscopy characterization of the catalysts was performed at $150^\circ C$ under ultrahigh vacuum by using a Bruker EQUINOX55 infrared spectrometer. Nitrogen adsorption and desorption isotherms were determined with a Micromeritics apparatus of model ASAP-2050 system at $-196^\circ C$. The specific surface areas were calculated by the BET method, and the pore-size distributions were calculated from the adsorption branch of the isotherm by the BJH model.

Catalytic performance measurements

Direct dehydrogenation of ethylbenzene was performed at $550^\circ C$ for 20 h in a stainless steel, fixed-bed flow reactor (10 mm O.D.). The catalyst (25 mg) was placed at the center of the reactor by using quartz wool plugs at its two sides. The system was heated at $600^\circ C$ for 30 min under an atmosphere of Ar as the pretreatment process. After the system was cooled down to $550^\circ C$ and kept at that temperature for 10 min, 2.8% ethylbenzene with a feed flow rate of 10 mL min^{-1} and Ar as balance was then fed into the reactor from a saturator kept at $40^\circ C$. The effluent from the reactor was condensed in two traps containing ethanol connected in a series. The condensed material was cooled externally in an ice water bath. Quantitative analysis of the collected reaction products (ethylbenzene, styrene, toluene, and benzene) was performed with a FULI 9790 II GC equipped with an HP-5 column, $30 \text{ m} \times 0.32 \text{ mm} \times 0.25 \mu m$, and a flame ionization detector. The resulting carbon balance was above $(100 \pm 4)\%$ in all reactions. The conversion of ethylbenzene (X_{EB}) [Eq. (2)], yield of styrene (Y_{EB}) [Eq. (3)],

and the selectivity of styrene (S_{ST}) [Eq. (4)] were calculated as follows (EB, ST, BZ, and TOL are denoted as ethylbenzene, styrene, benzene, and toluene, respectively):

$$X_{EB} [\%] = \left(1 - \frac{n_{EB,outlet}}{n_{EB,inlet}}\right) \times 100 \quad (2)$$

$$Y_{EB} [\%] = \frac{n_{ST,outlet}}{n_{EB,inlet}} \times 100 \quad (3)$$

$$S_{ST} [\%] = \frac{n_{ST,outlet}}{(n_{ST,outlet} + n_{BZ,outlet} + n_{TOL,outlet})} \times 100 \quad (4)$$

Electrocatalytic performance in oxygen reduction

The sample (4 mg) was dispersed in ethanol (2.0 mL). The mixture was ultrasonicated to obtain a homogenous catalyst ink. To prepare the working electrode for electrochemical measurements, the ink (20 μL) was dipped on a mirror-polished glass carbon electrode and dried at $25^\circ C$ in air (4 \times); this was followed by casting with a Nafion solution (5 wt% in isopropanol). Then, the working electrode was inserted into the cell setup, which was composed of a platinum counter electrode, an Hg/Hg₂Cl₂ reference electrode, and a 125 mL glass cell containing 0.1 M KOH aqueous electrolyte (80 mL). Cyclic voltammetry experiments were performed with an electrochemical analysis station (CHI 650 D, Shanghai Chenhua Instrument Co., China). Before testing, an O₂/N₂ flow was used through the electrolyte in the cell for 20 min to saturate it with O₂/N₂. The cell was kept in a $25^\circ C$ water bath for all the electrochemical tests. Cyclic voltammetry was performed from 0.2 to -1.0 V versus Hg/Hg₂Cl₂, at a sweep rate of 50 mV s^{-1} . The sample was tested three times to avoid any incidental error. For the rotating disk electrode test, the same amount of catalyst was loaded on a rotating glass carbon electrode (Princeton Applied Research). Electrochemical measurements were performed with a CHI 650 D electrochemical workstation. A Pt wire and Hg/Hg₂Cl₂ were used as the counter and reference electrodes, respectively. The linear sweep voltammograms of the modified glass carbon electrode were recorded in O₂-saturated 0.1 M KOH at a scan rate of 10 mV s^{-1} at various rotating speeds from 400 to 2500 rpm. After each scan, the electrolyte was saturated with O₂ again for 20 min. The sample was tested three times to avoid any incidental error.

Acknowledgements

This work was financially supported by the National Natural Science Foundation of China (grant no. 20803006 and 21276041), the Joint Fund of Coal, set up by National Natural Science Foundation of China and Shenhua Co., Ltd. (No. U1261104), and also sponsored by the Chinese Ministry of Education through the Program for New Century Excellent Talents in University (Grant no. NCET-12-0079).

Keywords: dehydrogenation • dispersant and precursor • doping • hybrid nanocomposites • oxygen reduction reaction

[1] a) M. S. Chen, M. C. White, *Science* **2010**, 327, 566; b) L. Kesavan, R. Tiruvalam, M. Ab Rahim, M. I. bin Saiman, D. I. Enache, R. L. Jenkins, N. Dimitratos, J. A. Lopez-Sanchez, S. H. Taylor, D. W. Knight, C. J. Kiely, G. J. Hutchings, *Science* **2011**, 331, 195.

[2] a) J. Zhang, D. S. Su, R. Blume, R. Schlögl, R. Wang, X. Yang, A. Gajović, *Angew. Chem. Int. Ed.* **2010**, 49, 8640; *Angew. Chem.* **2010**, 122, 8822;

- b) Z. K. Zhao, Y. T. Dai, J. H. Lin, G. R. Wang, *Chem. Mater.* **2014**, *26*, 3151; c) Z. K. Zhao, Y. T. Dai, *J. Mater. Chem. A* **2014**, *2*, 13442; d) Y. Gao, G. Hu, J. Zhong, Z. Shi, Y. Zhu, D. S. Su, J. Wang, X. Bao, D. Ma, *Angew. Chem. Int. Ed.* **2013**, *52*, 2109; *Angew. Chem.* **2013**, *125*, 2163.
- [3] a) K. Schwinghammer, B. Tuffy, M. B. Mesch, E. Wirnhier, C. Martineau, F. Taulelle, W. Schnick, J. Senker, B. V. Lotsch, *Angew. Chem. Int. Ed.* **2013**, *52*, 2435; *Angew. Chem.* **2013**, *125*, 2495; b) X. Wang, K. Maeda, A. Thomas, K. Takanabe, G. Xin, J. M. Carlsson, K. Domen, M. Antonietti, *Nat. Mater.* **2009**, *8*, 76.
- [4] a) M. Shalom, S. Inal, C. Fetzkenhauer, D. Neher, M. Antonietti, *J. Am. Chem. Soc.* **2013**, *135*, 7118; b) Y. S. Jun, E. Z. Lee, X. Wang, W. H. Hong, G. D. Stucky, A. Thomas, *Adv. Funct. Mater.* **2013**, *23*, 3661.
- [5] a) P. Chen, T. Y. Xiao, Y. H. Qian, S. S. Li, S. H. Yu, *Adv. Mater.* **2013**, *25*, 3192; b) Y. Zheng, Y. Jiao, L. Ge, M. Jaroniec, S. Z. Qiao, *Angew. Chem. Int. Ed.* **2013**, *52*, 3110; *Angew. Chem.* **2013**, *125*, 3192; c) Y. Zhao, L. Yang, S. Chen, X. Wang, Y. Ma, Q. Wu, Y. Jiang, W. Qian, Z. Hu, *J. Am. Chem. Soc.* **2013**, *135*, 1201.
- [6] a) S. Navalon, A. Dhakshinamoorthy, M. Alvaro, H. Garcia, *Chem. Rev.* **2014**, *114*, 6179; b) N. G. Sahoo, Y. Pan, L. Li, S. H. Chan, *Adv. Mater.* **2012**, *24*, 4203; c) D. R. Dreyer, C. W. Bielawski, *Chem. Sci.* **2011**, *2*, 1233; d) C. Huang, C. Li, G. Shi, *Energy Environ. Sci.* **2012**, *5*, 8848; e) C. Su, K. P. Loh, *Acc. Chem. Res.* **2013**, *46*, 2275.
- [7] a) K. S. Novoselov, A. K. Geim, S. V. Morozov, D. Jiang, Y. Zhang, S. V. Dubonos, I. V. Grigorieva, A. A. Firsov, *Science* **2004**, *306*, 666; b) D. Krishnan, F. Kim, J. Luo, R. Cruz-Silva, L. J. Cote, H. D. Jang, J. Huang, *Nano Today* **2012**, *7*, 137; c) P. Wu, Z. Cai, Y. Gao, H. Zhang, C. Cai, *Chem. Commun.* **2011**, *47*, 11327; d) Y. Wang, Y. Shao, D. W. Matson, D. J. Li, Y. Lin, *ACS Nano* **2010**, *4*, 1790.
- [8] a) D. Zhang, T. Yan, L. Shi, Z. Peng, X. Wen, J. Zhang, *J. Mater. Chem.* **2012**, *22*, 14696; b) M. Beidaghi, C. Wang, *Adv. Funct. Mater.* **2012**, *22*, 4501; c) K. J. Koski, Y. Cui, *ACS Nano* **2013**, *7*, 3739; d) Z. P. Chen, W. C. Ren, L. B. Gao, B. L. Liu, S. F. Pei, H. M. Cheng, *Nat. Mater.* **2011**, *10*, 424; e) Y. Sun, Q. Wu, Y. Xu, H. Bai, C. Li, G. Shi, *J. Mater. Chem.* **2011**, *21*, 7154.
- [9] V. Danilenko, *Phys. Solid State* **2004**, *46*, 595.
- [10] a) X. Q. Zhang, R. Lam, X. Xu, E. K. Chow, H. J. Kim, D. Ho, *Adv. Mater.* **2011**, *23*, 4770; b) W. Yang, O. Auciello, J. E. Butler, W. Cai, J. A. Carlisle, J. E. Gerbi, D. M. Gruen, T. Knickerbocker, T. L. Lasseter, J. N. Russell, L. M. Smith, R. J. Hamers, *Nat. Mater.* **2002**, *1*, 253; c) V. N. Mochalin, Y. Gogotsi, *J. Am. Chem. Soc.* **2009**, *131*, 4594.
- [11] a) C. Wang, J. Chen, G. Yang, N. Xu, *Angew. Chem. Int. Ed.* **2005**, *44*, 7414; *Angew. Chem.* **2005**, *117*, 7580; b) B. T. Branson, M. A. Seif, J. L. Davidson, C. M. Lukehart, *J. Mater. Chem.* **2011**, *21*, 18832; c) V. N. Mochalin, O. Shenderova, D. Ho, Y. Gogotsi, *Nat. Nanotechnol.* **2012**, *7*, 11.
- [12] a) X. H. Li, M. Antonietti, *Angew. Chem. Int. Ed.* **2013**, *52*, 4572; *Angew. Chem.* **2013**, *125*, 4670; b) J. Liang, X. Du, C. Gibson, X. W. Du, S. Z. Qiao, *Adv. Mater.* **2013**, *25*, 6226; c) B. Frank, J. Zhang, R. Blume, R. Schlügl, D. S. Su, *Angew. Chem. Int. Ed.* **2009**, *48*, 6913; *Angew. Chem.* **2009**, *121*, 7046; d) F. Gao, G. L. Zhao, S. Yang, J. J. Spivey, *J. Am. Chem. Soc.* **2013**, *135*, 3315; e) J. P. Paraknowitsch, A. Thomas, *Energy Environ. Sci.* **2013**, *6*, 2839.
- [13] W. S. Hummers, R. E. Offeman, *J. Am. Chem. Soc.* **1958**, *80*, 1339.
- [14] a) S. Tomita, A. Burian, J. C. Dore, D. LeBolloch, M. Fujii, S. Hayashi, *Carbon* **2002**, *40*, 1469; b) O. O. Mykhaylyk, Y. M. Solonin, D. N. Batchelder, R. Brydson, *J. Appl. Phys.* **2005**, *97*, 074302; c) J. Chen, S. Z. Deng, J. Chen, Z. X. Yu, N. S. Xu, *Appl. Phys. Lett.* **1999**, *74*, 3651.
- [15] a) N. Jung, S. Kwon, D. Lee, D. M. Yoon, Y. M. Park, A. Benayad, J. Y. Choi, J. S. Park, *Adv. Mater.* **2013**, *25*, 6854; b) L. Feng, Y. Chen, L. Chen, *ACS Nano* **2011**, *5*, 9611.
- [16] a) Z. Guo, J. Wang, F. Wang, D. Zhou, Y. Xia, Y. Wang, *Adv. Funct. Mater.* **2013**, *23*, 4840; b) J. H. Lee, N. Park, B. G. Kim, D. S. Jung, K. Im, J. Hur, J. W. Choi, *ACS Nano* **2013**, *7*, 9366.
- [17] a) J. Liang, Y. Jiao, M. Jaroniec, S. Z. Qiao, *Angew. Chem. Int. Ed.* **2012**, *51*, 11496; *Angew. Chem.* **2012**, *124*, 11664; b) J. Y. Kim, W. H. Lee, J. W. Suk, J. R. Potts, H. Chou, I. N. Kholmanov, R. D. Piner, J. Lee, D. Akinwande, R. S. Ruoff, *Adv. Mater.* **2013**, *25*, 2308; c) C. Zhang, L. Fu, N. Liu, M. Liu, Y. Wang, Z. Liu, *Adv. Mater.* **2011**, *23*, 1020; d) B. Guo, Q. Liu, E. Chen, H. Zhu, L. Fang, J. R. Gong, *Nano Lett.* **2010**, *10*, 4975; e) P. Wu, Y. Qian, P. Du, H. Zhang, C. Cai, *J. Mater. Chem.* **2012**, *22*, 6402.
- [18] a) Z. H. Sheng, L. Shao, J. J. Chen, W. J. Bao, F. B. Wang, X. H. Xi, *ACS Nano* **2011**, *5*, 4350; b) G. H. Jun, S. H. Jin, B. Lee, B. H. Kim, W. S. Chae, S. H. Hong, S. Jeon, *Energy Environ. Sci.* **2013**, *6*, 3000.
- [19] a) Z. Lin, G. Waller, Y. Liu, M. Liu, C. P. Wong, *Adv. Energy Mater.* **2012**, *2*, 884; b) Z. Jin, J. Yao, C. Kittrell, J. M. Tour, *ACS Nano* **2011**, *5*, 4112; c) I. V. Lightcap, P. V. Kamat, *Acc. Chem. Res.* **2013**, *46*, 2235.
- [20] a) Y. Li, Y. Zhao, H. Cheng, Y. Hu, G. Shi, L. Dai, L. Qu, *J. Am. Chem. Soc.* **2012**, *134*, 15; b) L. Shang, T. Bian, B. Zhang, D. Zhang, L. Z. Wu, C. H. Tung, Y. Yin, T. Zhang, *Angew. Chem. Int. Ed.* **2014**, *53*, 250; *Angew. Chem.* **2014**, *126*, 254.
- [21] a) W. Ding, Z. Wei, S. Chen, X. Qi, T. Yang, J. Hu, D. Wang, L. J. Wan, *Angew. Chem. Int. Ed.* **2013**, *52*, 11755; *Angew. Chem.* **2013**, *125*, 11971; b) X. H. Li, S. Kurasch, U. Kaiser, M. Antonietti, *Angew. Chem. Int. Ed.* **2012**, *51*, 9689; *Angew. Chem.* **2012**, *124*, 9827.
- [22] a) W. Qi, W. Liu, B. Zhang, X. Gu, X. Guo, D. Su, *Angew. Chem. Int. Ed.* **2013**, *52*, 14224; *Angew. Chem.* **2013**, *125*, 14474; b) Y. Hou, Z. Wen, S. Cui, X. Guo, J. Chen, *Adv. Mater.* **2013**, *25*, 6291; c) T. N. Huan, T. V. Khai, Y. Kang, K. B. Shim, H. Chung, *J. Mater. Chem.* **2012**, *22*, 14756.
- [23] a) N. Xiao, Y. Zhou, Z. Ling, Z. Zhao, J. Qiu, *Carbon* **2013**, *60*, 514; b) C. Liang, H. Xie, V. Schwartz, J. Howe, S. Dai, S. H. Overbury, *J. Am. Chem. Soc.* **2009**, *131*, 7735; c) R. Rao, M. Yang, Q. Ling, C. Li, Q. Zhang, H. Yang, *Catal. Sci. Technol.* **2014**, *4*, 665; d) G. Xie, K. Zhang, B. Guo, Q. Liu, L. Fang, J. R. Gong, *Adv. Mater.* **2013**, *25*, 3820.
- [24] a) I. Katsounaros, S. Cherevko, A. R. Zeradjanin, K. J. J. Mayrhofer, *Angew. Chem. Int. Ed.* **2014**, *53*, 102; *Angew. Chem.* **2014**, *126*, 104; b) F. Cheng, J. Chen, *Chem. Soc. Rev.* **2012**, *41*, 2172; c) Y. J. Sa, C. Park, H. Y. Jeong, S. H. Park, Z. Lee, K. T. Kim, G. G. Park, S. H. Joo, *Angew. Chem. Int. Ed.* **2014**, *53*, 4102; *Angew. Chem.* **2014**, *126*, 4186.

Received: January 27, 2015

Published online on ■■■■■, 0000



A sparkling discovery: A N-doped mesoporous graphene/nanodiamond (N-RGO/ND) hybrid nanocomposite is fabricated by a facile and scalable wet-chemical approach. The nanocomposite shows excellent activity in the thermo-

catalytic direct dehydrogenation of ethylbenzene and in the electrocatalytic oxygen reduction reaction, which can be ascribed to the unique structure and surface chemical properties of the nanocomposite.

Z. Zhao,* Y. Dai, G. Ge, Q. Mao, Z. Rong, G. Wang



A Facile Approach to Fabricate an N-Doped Mesoporous Graphene/Nanodiamond Hybrid Nanocomposite with Synergistically Enhanced Catalysis

